JACS
JOURNAL OF THE AMERICAN CHEMICAL SOCIETY
Article
pubs.acs.org/JACS

Ternary Electrocatalysts for Oxidizing Ethanol to Carbon Dioxide: Making Ir Capable of Splitting C−C Bond

Meng Li,[†] David A. Cullen,[‡] Kotaro Sasaki,[†] Nebojsa S. Marinkovic,[§] Karren More,[‡] and Radoslav R. Adzic*[,†]

[†]Department of Chemistry, Brookhaven National Laboratory, Upton, New York 11973, United States
[‡]Materials Science and Technology Division, Oak Ridge National Laboratory, Oak Ridge, Tennessee 37831, United States
[§]Departmant of Chemical Engineering, University of Delaware, Newark, Delaware 19716, United States

Supporting Information

ABSTRACT: Splitting the C−C bond is the main obstacle to electrooxidation of ethanol (EOR) to CO_2. We recently demonstrated that the ternary $PtRhSnO_2$ electrocatalyst can accomplish that reaction at room temperature with Rh having a unique capability to split the C−C bond. In this article, we report the finding that Ir can be induced to split the C−C bond as a component of the ternary catalyst. We characterized and compared the properties of several carbon-supported nanoparticle (NP) electrocatalysts comprising a SnO_2 NP core decorated with multimetallic nanoislands (MM′ = PtIr, PtRh, IrRh, PtIrRh) prepared using a seeded growth approach. An array of characterization techniques were employed to establish the composition and architecture of the synthesized MM′/SnO_2 NPs, while electrochemical and *in situ* infrared reflection absorption spectroscopy studies elucidated trends in activity and the nature of the reaction intermediates and products. Both EOR reactivity and selectivity toward CO_2 formation of several of these MM′/SnO_2/C electrocatalysts are significantly higher compared to conventional Pt/C and Pt/SnO_2/C catalysts. We demonstrate that the PtIr/SnO_2/C catalyst with high Ir content shows outstanding catalytic properties with the most negative EOR onset potential and reasonably good selectivity toward ethanol complete oxidation to CO_2.

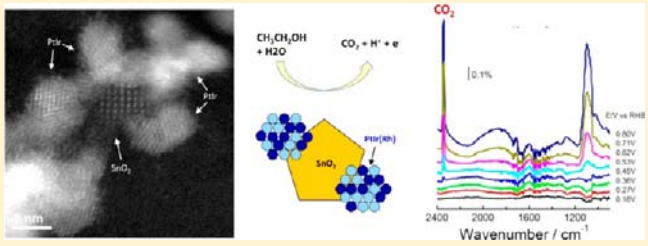

1. INTRODUCTION

Finite resources of fossil fuels and environmental concerns are currently stimulating a broad, intensive search for alternative energy sources. Ethanol is one of the most attractive sources of clean energy as it has several important properties for direct energy conversion applications,[1−3] including a high energy density of 8 kWh/kg, which is comparable to that of gasoline. It is nontoxic liquid and is easy to store and transport. Therefore, the direct ethanol fuel cell (DEFC) offers distinct potential advantages over internal combustion engines and hydrogen fuel cells for transportation and residential applications. In addition, ethanol can be produced from renewable sources; for instance, ethanol can be easily produced in large quantities by the fermentation of cellulose-containing raw agriculture materials (e.g., corn, wheat, sugar beet, sugar cane, etc.).[3,4] However, one major impediment to the commercialization of DEFCs is that the ethanol oxidation reaction (EOR) occurring at the fuel cell anode is slow and incomplete, even on the best available electrocatalysts. This reaction generates several intermediates, and furthermore, the oxidation of ethanol to CO_2 is not fully completed, that is, the C−C bond is not broken. Pt can be improved by alloying with a second metal (e.g., Ru, Sn, etc.) that can provide oxygen containing species (i.e., OH) at low potentials for oxidation of poisoning intermediates (i.e., CO), but despite some improvements,[4−12] so far, there is still no efficient catalyst for ethanol electrooxidation.[13−17]

Thus, the major challenge for the electrocatalysis of ethanol is to split the C−C bond and to oxidize ethanol to CO_2 at low overpotentials. Our group developed the multifunctional ternary Pt−Rh−SnO_2 electrocatalyst which is effective in splitting the C−C bond in ethanol at room temperature,[18,19] and the catalytic property of the ternary catalyst is attributed to the synergistic effect between all three constituents (where Pt is liable for ethanol dehydrogenerative adsorption, SnO_2 supplies oxygen-containing species and Rh is responsible for C−C bond cleavage[20−22]). The combined density functional theory (DFT) and kinetic Monte Carlo (kMC) simulations conducted by Choi et al.[23] proposed that ethanol on Rh(111) is decomposed into C and CO, with the cleavage of the C−C bonds. Rh is one of the rarest and most costly precious metals; hence, to optimize and reduce Rh content and eventually to replace Rh is of great importance in designing practical ethanol oxidation catalysts. In this study, we explored Ir as an alternative to Rh in the ternary system to form a highly efficient EOR catalyst. Ir is in the same group as Rh; therefore, it is expected that the two may have similar adsorptive and catalytic properties.[24] Surface

Received: July 1, 2012
Published: December 4, 2012

   dx.doi.org/10.1021/ja306384x | J. Am. Chem. Soc. 2013, 135, 132−141

science studies revealed similarities between pathways of ethanol decomposition on Ir(111) and Rh(111).[20,25] *In situ* infrared study of ethanol electrooxidation on a polycrystalline Ir electrode showed the existence of adsorbed CO and solution phase CO_2, indicating the C−C bond can be broken on Ir.[24] Moreover, attempts have been made to study Ir-containing catalysts such as Ir and Ir_3Sn nanoparticle catalysts and these catalysts showed promising performance in DEFC tests.[10,26] Lastly, Ir is one of the most stable and corrosion-resistant metal known, making it suitable for fuel cell applications.

In this work, special attention has been focused on investigating Ir in the ternary system as an alternative to Rh, as well as the optimization of ternary catalysts. We report on our DFT calculation guided design, syntheses, and characterization of carbon-supported MM′/SnO_2 NPs consisting of multimetallic nanoislands (MM′ = PtIr, PtRh, IrRh, PtIrRh) deposited on SnO_2 NP cores, which provide active metal−metal oxide interfaces and are synthetic analogues of the PtRh/SnO_2(110) model catalyst in our earlier DFT study.[18] We first employed a range of characterization techniques, including inductively coupled plasma optical emission spectroscopy (ICP-OES), X-ray diffraction (XRD), Z-contrast aberration-corrected scanning transmission electron microscopy (AC-STEM) coupled with energy disperse X-ray spectroscopy (EDS) and *in situ* X-ray absorption spectroscopy (XAS), to establish the composition and architecture of the synthesized MM′/SnO_2 NPs. Carbon-supported MM′/SnO_2 electrocatalysts with different compositions were prepared using a seeded growth approach and investigated using a combination of electrochemical methods and *in situ* infrared reflection absorption spectroscopy (IRRAS) to elucidate the correlations between the chemical composition and catalytic properties (activity and selectivity) of the electrocatalysts in ethanol electrooxidation. We demonstrate that optimized PtIr/SnO_2/C and PtRh/SnO_2/C electrocatalysts exhibit very high EOR activity and selectivity toward the complete oxidation of ethanol to CO_2. These findings are of great importance in terms of understanding and designing novel nanostructured materials with substantially improved activity and selectivity in ethanol oxidation.

2. METHODS

2.1. Materials Preparation. The carbon-supported MM′/SnO_2 NP catalysts were prepared using a seeded growth approach with SnO_2 NPs being formed first and then multimetallic (MM′ = PtIr, PtRh, IrRh or PtIrRh) nanoislands being reduced on SnO_2 NP substrates afterward. Chemicals, $PtCl_4$, $(NH4)_2IrCl_6$, $RhCl_3$, $SnCl_2{\cdot}2H_2O$, ethylene glycol (EG), and sodium hydroxide (NaOH) were purchased and used as received.

2.1.1. Synthesis of SnO_2 NPs. In a typical procedure, calculated amounts of $SnCl_2{\cdot}2H_2O$ were dissolved in the mixture of 99 mL of EG and 1 mL of H_2O to form a clear solution. Temperature was ramped to 190 °C and was kept there for 1 h with oxygen flowing in the flask. The resulting SnO_2 colloid with a light yellow color was then cooled to room temperature.

2.1.2. PtIr/SnO_2 NPs. Suitable amounts of $PtCl_4$ and $(NH_4)_2IrCl_6$ were dissolved in 40 mL of EG first and then added to the SnO_2 colloid. Concentrated NaOH solution (10 M in water) was used to raise the pH value to 13. The mixture was slowly heated to 130 °C with a temperature ramp of around 1 °C/min and kept at 130 °C for 2 h. After cooling to room temperature, concentrated sulfuric acid (98% H_2SO_4) was added to adjust the pH value to neutral. The reaction was carried out under argon atmosphere. Three PtIr/SnO_2 NP catalysts with atomic ratio Pt/Ir/Sn of 1:1:1, 1:$^1/_2$:1, and 1:$^1/_4$:1 were prepared.

2.1.3. PtRh/SnO_2, IrRh/SnO_2 and PtIrRh/SnO_2 NPs. Three categories of electrocatalysts, PtRh/SnO_2, IrRh/SnO_2, and PtIrRh/SnO_2, were synthesized in a similar fashion as PtIr/SnO_2. Four PtRh/SnO_2 NP catalysts with atomic ratio Pt/Rh/Sn of 1:1:1, 1:$^1/_2$:1, 1:$^1/_3$:1, and 1:$^1/_4$:1; one IrRh/SnO_2 NP catalyst with atomic ratio Ir/Rh/Sn of 1:1:1; and one PtIrRh/SnO_2 NP catalyst with atomic ratio Pt/Ir/Rh/Sn of 1:1:1:1 were prepared.

2.1.4. Preparation of Carbon-Supported Electrocatalysts. The resulting black colloid containing MM′/SnO_2 NPs suspended in EG was first cooled to room temperature, then a calculated amount of Vulcan XC-72 carbon black was added, and the mixture was stirred overnight. The resulting slurry was filtered, washed first with ethanol and then with copious distilled water, and the precipitate was dried in a vacuum oven at 80 °C overnight. The catalysts were annealed in argon at 200 °C for 1 h to remove remaining EG. All of the above electrocatalysts were prepared with a 40% loading on Vulcan carbon support.

2.2. Composition and Structure Characterization. Catalysts' actual chemical composition was studied by ICP-OES and *in situ* XAS. The crystalline structures of the electrocatalysts were studied using XRD with an X-ray wavelength of 0.3184 Å at beamline X7B in the National Synchrotron Light Source (NSLS) at Brookhaven National Laboratory (BNL). Z-contrast AC-STEM imaging coupled with EDS mapping was performed in a JEOL JEM-2200FS at Oak Ridge National Laboratory to determine the composition and architecture of the synthesized NP electrocatalysts.

2.3. Electrochemical Measurements. A VoltaLab PGZ100 potentiostat was employed for the electrochemical measurements in a standard three-electrode electrochemical cell. A total of 5 mg of electrocatalysts was ultrasonically mixed with a 2 mL of ethanol/water solution (volume ratio 1:1) to form a uniform ink and 5 μL of ink was pipetted onto the polished glassy carbon (GC) disk to form a homogeneous thin catalyst layer. Both cyclic voltammetry (CV) and chronoamperometry (CA) measurements in ethanol-containing solution were carried out to evaluate the EOR reactivity of each catalyst. The measurements were performed at room temperature, and the potentials given in this paper were referenced to that of the reversible hydrogen electrode (RHE).

2.4. *In Situ* Infrared Reflection Absorption Spectroscopy (IRRAS). *In situ* IRRAS studies were carried out with a Nicolet Nexus 670 FT-IR spectrometer equipped with a MCT detector cooled with liquid nitrogen. An unpolarized light beam was used. The spectral resolution was set to 8 cm^{-1} and 128 interferograms were together added to each spectrum. Spectra are given in absorbance units defined as $A = -\log(R/R_0)$, where R and R_0 represent the reflected IR intensities corresponding to the sample- and reference single beam spectrum, respectively. Working electrodes used in this IR study were prepared following the same method as those used in the electrochemical studies, with 20 μL of catalyst ink deposited on a polished polycrystalline Au disk to form a homogeneous catalyst layer. A ZnSe hemisphere was used as the IR window, and the working electrodes used in this IR study, including PtIr/SnO_2/C, PtRh/SnO_2/C, and PtIrRh/SnO_2/C electrocatalysts with different compositions, were pressed against the IR window to create a thin electrolyte layer with a thickness of a few micrometers. Pure Ar and dry air were used to purge the electrolyte and spectrometer, respectively, to remove the spectral interference from CO_2 and water vapor present in air. Reference spectra were collected in 0.05 V versus RHE in the same solution with 0.1 M ethanol and 0.1 M $HClO_4$, and all the sample spectra were collected at different applied potentials.

2.5. *In Situ* X-ray Absorption Spectroscopy (XAS). *In situ* XAS measurements were conducted at the L-3 edges for Pt and Ir at beamline X18B in the NSLS at BNL. Carbon-supported PtIr/SnO_2 catalyst with a Pt/Ir/Sn atomic ratio of 1:1:1 was pressed on a membrane as a working electrode and sealed in a Plexiglas cell, equipped with a conventional three electrode system. The details on the *in situ* XAS spectro-electrochemical cell for spectroscopic measurements in both fluorescence and transmission mode are described elsewhere[27] as well as on the Synchrotron Catalysis Consortium web page (http://www.yu.edu/scc/). XAS spectra were

dx.doi.org/10.1021/ja306384x | J. Am. Chem. Soc. 2013, 135, 132−141

collected at specific potentials between hydrogen and oxygen evolution regions in steps of 0.2 V, in a steady-state potential mode, allowing ~2 min for current stabilization. The XAS data were processed using Athena analysis program.[28]

3. RESULTS

3.1. Physical Characterization. The heteronanostructured MM′/SnO_2 NP electrocatalysts comprised of SnO_2 NP cores decorated with multimetallic (MM′) nanoislands (MM′ = PtIr, PtRh, IrRh, or PtIrRh) were prepared as direct analogues of the PtRh/SnO_2(110) model catalyst. SnO_2 NPs were synthesized using modified known methods,[29,30] with $SnCl_2$ being reduced to form Sn^0 by heating in EG, then quickly being oxidized to SnO_2 afterward in the O_2 flow. Multimetallic nanoislands were subsequently deposited on the preformed SnO_2 NP seeds using chloride precursors ($PtCl_4$, $(NH_4)_2IrCl_6$ and/or $RhCl_3$) and a seeded growth technique (Figure 1). Most recently, seeded

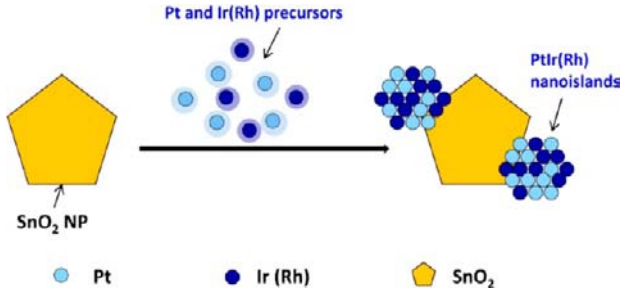

Figure 1. Schematic illustration of the synthesis of MM′/SnO_2 nanoparticles using a seeded growth approach.

growth has emerged for precisely controlling the morphology and composition of metallic nanostructures that are prepared using solution-phase methods.[31−33] It has been stated that in a system with pre-existing core particles, the critical energy barrier is generally smaller for heterogeneous nucleation of solute atoms than that for homogeneous one, and if sufficient sites are available for heterogeneous nucleation, both the number of critical clusters and nucleation rate should be larger for heterogeneous nucleation than for homogeneous.[33] In other words, the solute atoms will tend to nucleate and grow heterogeneously. A range of complex nanostructures have been synthesized using the seeded growth technique, such as core−shell, dumbbell, and particle-on-particle structures.[31−36] Although most reported cases are metal-on-metal growth, it has been claimed that a thin RuO_2 shell covering the Ru^0 core is necessary for Pt coating in the formation of Ru@Pt core−shell nanoparticles.[31] Because of the large lattice mismatch between metals (Pt, Ir and Rh) and the SnO_2 NP substrates, metal islands are expected to grow on those high energy sites of the substrate NPs and form islands in order to minimize strain energy, following the so-called Volmer−Weber (VW) or island growth mode.[33] The growth of the metal nucleus results in spherical shape and sometimes chain-like metal nanoislands, as observed by AC-STEM imaging (Figure 2). The surfactant-free syntheses were conducted with EG serving as both reducing agent and stabilizer, in order to retain clean surfaces for electrochemical reactions.

The synthesized MM′/SnO_2/C catalysts were characterized using several analytical methods. The atomic structures and elemental distributions of MM′/SnO_2 NPs were examined using Z-contrast AC-STEM coupled with EDS mapping. Z-contrast STEM is more commonly referred to as high-angle annular dark-field (HAADF) STEM, and the contrast/brightness observed in Z-contrast images is approximately proportional to the total number of atoms in the column (or the thickness of the particle) and the square of their average atomic number (Z^2).

Figure 2 includes typical Z-contrast AC-STEM images of three MM′/SnO_2/C catalysts. PtIr (PtRh) nanoislands appear bright on the dark carbon background and SnO_2 NPs appear as light gray "rafts" beneath the PtIr nanoislands because Pt and Ir have larger atomic numbers (Z value) than Sn and O. One atomically resolved AC-STEM image (Figure 2a) of PtIrSnO_2/C catalyst (with atomic ratio Pt/Ir/Sn of 1:1:1) clearly shows several PtIr spherical-shaped nanoislands decorating a crystalline SnO_2 NP substrate. Fringes in the SnO_2 NP show a lattice spacing of about 3.35 Å, corresponding to the (110) family of SnO_2 lattice planes. In Figure 2d, PtIr clusters form chain-like nanoislands deposited on semicrystalline SnO_2 NP substrates. Careful observations of more SnO_2 NPs showed the predominant lattice spacings are 2.64 Å (011 planes) and 3.35 Å (110 planes). The study on PtIr nanoislands showed a dominant fringe spacing of about 2.26 Å, which corresponds to (111) family of PtIr. Similar studies were carried out on all MM′/SnO_2/C NP samples, and the results confirm that the obtained nanocatalysts consisted of multimetallic (MM′ = PtRh, PtIr, IrRh, and PtIrRh) nanoislands decorating the SnO_2 NP substrates. More DF and brigh-field (BF) AC-STEM images from three MM′/SnO_2/C catalysts (PtIr/SnO_2/C, $PtRh_{1/2}$/SnO_2/C, and $PtRh_{1/3}$/SnO_2/C) are included in Figure S1, and they show an average diameter of PtIr and PtRh particles of about 2 nm. The size of SnO_2 NPs is more difficult to determine because of their irregular shapes and semicrystalline nature, and one can see they are usually in the range of 3−8 nm, which is larger than the multimetallic metal nanoislands.

Coupling element-sensitive EDS with Z-contrast AC-STEM images offers another way to determine the compositional distribution in MM′/SnO_2 NPs. Figure 3 shows a Z-contrast AC-STEM image with accompanying composite EDS elemental map. The superposed Pt, Ir, and Sn maps show that PtIr alloy nanoislands are decorating the SnO_2 NP supports in the PtIr/SnO_2/C catalyst (with atomic ratio Pt/Ir/Sn of 1:1:1). Similar analyses of two PtRh/SnO_2/C catalysts (with atomic ratio Pt/Rh/Sn as $1:^1/_2:1$ and $1:^1/_3:1$) are presented in Figure S2. Pt−Rh maps (Figure S2b,f) suggest that a random PtRh alloy is formed in both PtRh/SnO_2/C catalysts, as Pt and Rh signals are overlapping. The O-signal associated with Sn (Figure S2d) confirms that the broad rafts are tin oxide, instead of metallic tin. Pt−Sn maps (Figure S2c,g) demonstrate that PtRh nanoislands are deposited on SnO_2 NP substrates. In addition, STEM images taken before and after a 6 min EDS mapping indicate that the samples are sensitive to the high energy electron beam; hence, the mapping time was limited to 6 min. It should be noted that the relatively short mapping time limits our ability to acquire high quality EDS maps with sufficient counts to perform reliable quantitative analysis, but maps still show qualitatively the distribution of Pt, Ir, Rh and Sn.

Figure 4 presents XRD profiles of different carbon-supported MM′/SnO_2 (MM′ = PtIr and PtRh) NP catalysts. The broadening of diffraction peaks indicates all NP catalysts consisted of nanoparticles having a very small particle size, which is consistent with our STEM observations. Figure 4c displays XRD patterns of $PtRh_{1/2}$/SnO_2/C electrocatalyst and also Pt/SnO_2/C electrocatalyst (with atomic ratio Pt/Sn of

dx.doi.org/10.1021/ja306384x | J. Am. Chem. Soc. 2013, 135, 132−141

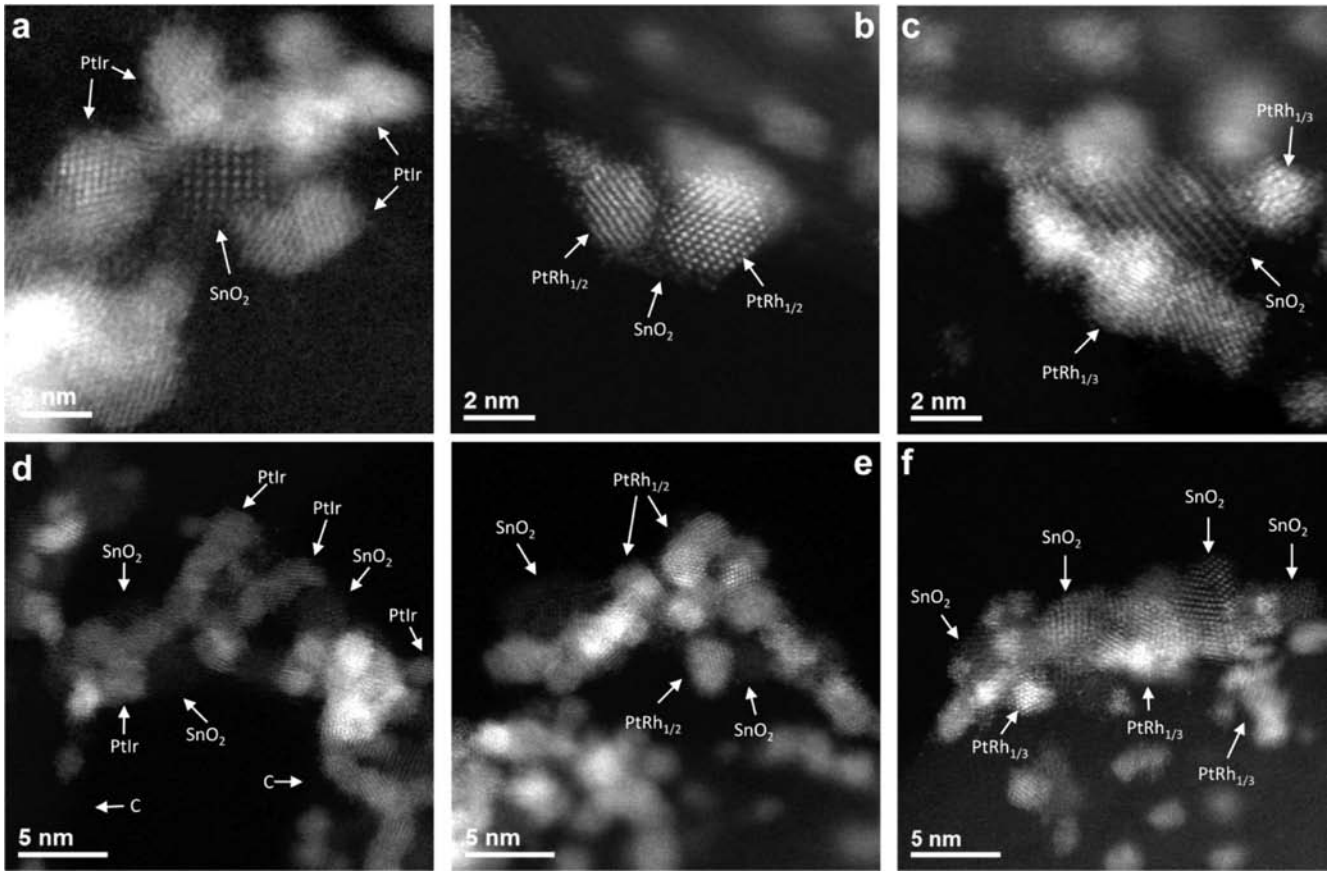

Figure 2. Representative high resolution Z-contrast AC-STEM images of $PtIr/SnO_2/C$ (a and d), $PtRh_{1/2}/SnO_2/C$ (b and e), and $PtRh_{1/3}/SnO_2/C$ (c and f) electrocatalysts.

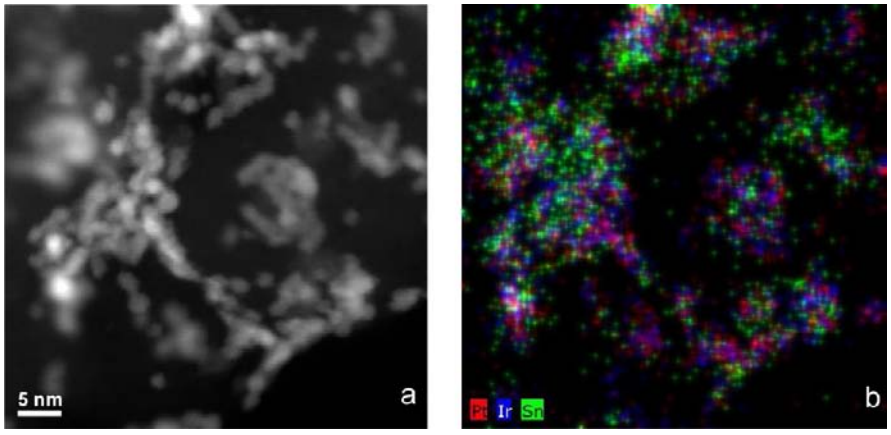

Figure 3. HAADF AC-STEM image and corresponding EDS elemental map of $PtIr/SnO_2/C$ electrocatalyst. See text for details.

1:1) prepared using the same method. Similar to our previous study,[18,19] Pt and Rh diffraction peaks cannot be resolved separately in the spectrum, suggesting the formation of a random PtRh alloy when combined with EDS mapping and EXAFS fitting results. From Figure 4d, one can observe the PtRh(111) peak position shifts to higher 2θ, consistent with a more compressed lattice due to the smaller lattice constant of Rh with respect to that of Pt (3.8031 and 3.9231 Å, for Rh and Pt, respectively). The lattice parameters of the PtRh alloy nanoislands can be determined by refining XRD spectra, and more detailed analyses are ongoing to reveal the correlation between the lattice parameter and the composition.

XRD spectra of three $PtIr/SnO_2/C$ and $Pt/SnO_2/C$ electrocatalysts are presented in Figure 4a,b. The iridium component complicates the spectra because: (i) the Pt−Rh phase diagram suggests the formation of uniform solid solution at all ratios, while the Pt−Ir phase diagram shows the phase segregation at low temperature;[37] (ii) EXAFS fitting is insufficient in determining the relative distribution of Pt and Ir because their lattice parameters are too close (3.9231 and 3.8391 Å, for Pt and Ir, respectively);[38] (iii) the broad and poorly resolved PtIr(111) peaks in Figure 4a indicate a less crystalline nature of PtIr nanoislands compared to PtRh. However, one can still observe the shift of PtIr(111) peaks to

dx.doi.org/10.1021/ja306384x | J. Am. Chem. Soc. 2013, 135, 132−141

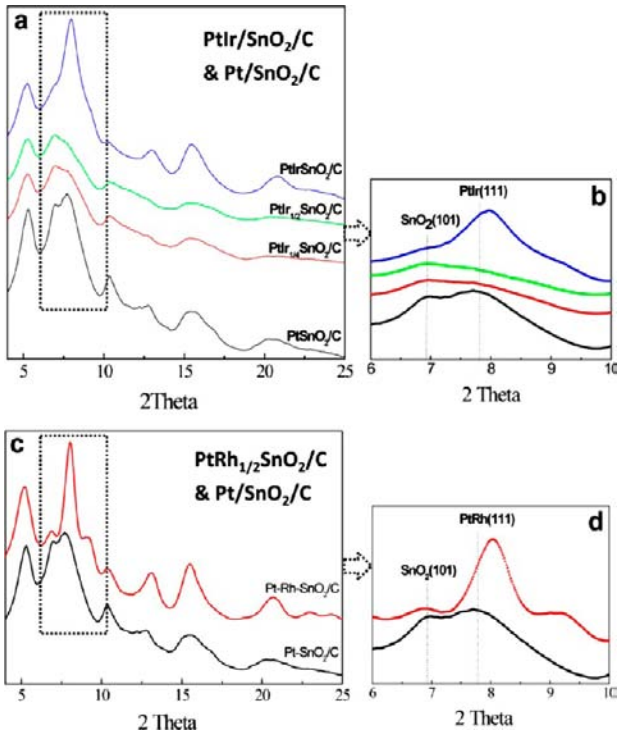

Figure 4. XRD profiles of different carbon-supported MM′/SnO_2 NP electrocatalysts. (a and b) PtIr/SnO_2 and Pt/SnO_2 NPs; (c and d) PtRh/SnO_2 and Pt/SnO_2 NPs.

higher 2θ values with increasing Ir content, indicating some degree of penetration of Ir atoms into the Pt lattice.

The chemical composition of the four PtRh/SnO_2/C catalysts was studied using ICP-OES (Table S1), and the Pt/Rh ratio in all four catalysts is present at a value close to the nominal one. Ir-containing catalysts were not subjected to ICP-OES study because Ir cannot be fully dissolved by aqua regia. However, *in situ* XAS study (discussed later) of PtIr/SnO_2/C (with atomic ratio Pt:Ir:Sn of 1:1:1) did suggest the atomic ratio Pt/Ir was close to 1, which approximates the nominal ratio (Pt/Ir of 1). Hence, the facile synthesis procedure achieves effective control in both structure and composition.

3.2. Electrochemical Measurements. Electrochemical voltammetric measurements were carried out to probe the surface information on the carbon-supported MM′/SnO_2 (MM′ = PtIr, PtRh, IrRh, or PtIrRh) electrocatalysts and evaluate their catalytic properties in ethanol electro-oxidation. In order to conduct a close comparison, all current density data shown were normalized to total noble metal mass, that is, the mass of Pt + Rh + Ir. Therefore, the observed trends in EOR activity directly reflects mass specific reactivity.

Voltammetry scans from three of PtIr/SnO_2/C catalysts (with atomic ratio Pt/Ir/Sn of 1:1:1, 1:$^1/_2$:1, and 1:$^1/_4$:1) in 0.1 M $HClO_4$ are included in Figure S3a. With increasing Ir content one can observe the enhanced surface oxide formation current and the negatively shifted oxide reduction potential. We attribute the variations to the alloying of Ir with Pt because Ir is less noble and more prone to oxidation with respect to Pt. The enlarged double layer current is due to the existence of iridium oxide (confirmed by XAS results). All three PtIr/SnO_2/C catalysts possess excellent EOR activity with a reaction onset potential just above 0.1 V, which is much lower than that of Pt/C and PtRu/C (0.4 and 0.3 V, respectively),[15] and a high current yield (Figure 5a). The hydrogen desorption feature is inhibited on all catalysts, indicating strong adsorption of

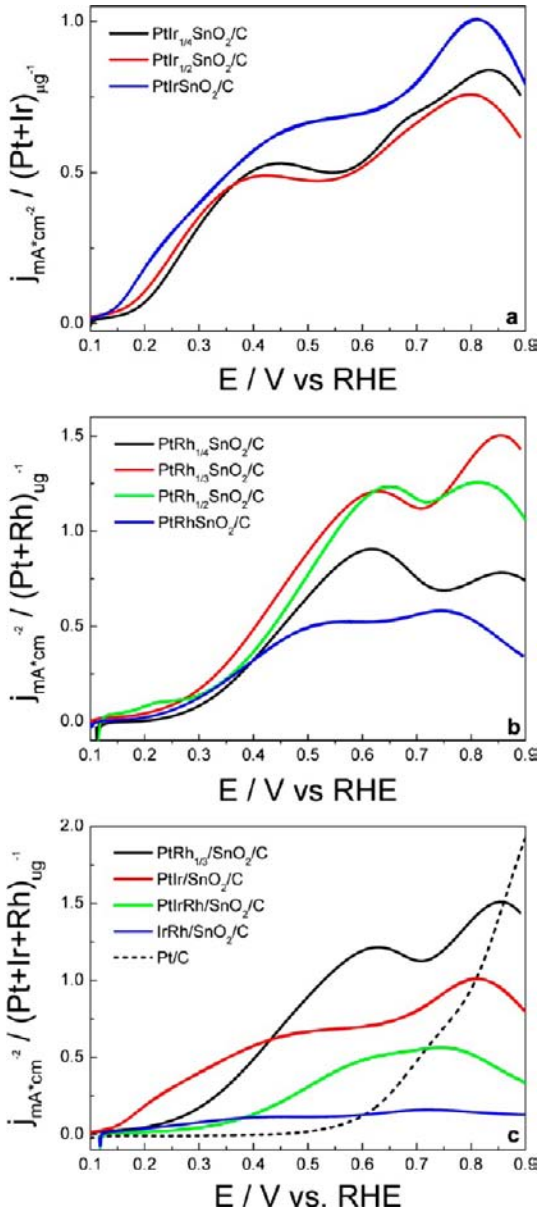

Figure 5. Anodic polarization curves for three PtIr/SnO_2/C (a), four PtRh/SnO_2/C (b), and PtIr/SnO_2/C, $PtRh_{1/3}$/SnO_2/C, IrRh/SnO_2/C, and PtIrRh/SnO_2/C (c) electrocatalysts in 0.1 M $HClO_4$ with 0.5 M ethanol and scan rate of 10 mV/C. The total noble metal mass (Pt + Rh + Ir) specific current densities were employed in the comparison, and all measurements were carried out at room temperature.

ethanol molecules on the active sites. The PtIr/SnO_2/C catalyst with highest Ir content, that is, atomic ratio Pt/Ir/Sn of 1:1:1, demonstrates the best activity. It has been observed that binary IrSn catalysts[10,26] show high activity in the low potential region, that is, 0.1−0.5 V; therefore, the high activity exhibited in PtIr/SnO_2/C with the highest Ir content can be attributed to the synergy between Ir and Sn.

Similar to PtIr/SnO_2/C catalysts, voltammetry curves of four PtRh/SnO_2/C catalysts (Figure S3b) show a systematic variation with the relative Pt/Rh ratio. The surface oxide formation on PtRh/SnO_2 NPs commences at around 0.35 V,

dx.doi.org/10.1021/ja306384x | J. Am. Chem. Soc. 2013, 135, 132−141

which is more negative than that observed on pure Pt NPs.[39] With increasing Rh content, one can find a larger current of oxygen adsorption and desorption and the surface oxide reduction peak potential shifts to more negative values. Figure 5b presents the anodic polarization curves of all the PtRh/SnO_2/C catalysts in ethanol-containing electrolyte. The profile demonstrates the onset potential of ethanol oxidation is just above 0.15 V. In these measurements the PtRh/SnO_2 catalysts with atomic ratio Pt/Rh/Sn of 1:$^1/_2$:1 and 1:$^1/_3$:1 show the best activity with the most negative EOR reaction onset potential and highest current yield. Hence, different from the observation in PtIr/SnO_2/C catalysts, a moderate Rh content gives the best EOR activity, while too high or too low Rh content causes a lowered activity.

PtIr/SnO_2/C catalysts further shift the reaction onset potential to more negative values compared to PtRh/SnO_2/C catalysts and it also shows improved CO_2 production with respect to Pt and Pt/SnO_2 catalysts (shown later). In addition, PtRh/SnO_2/C catalysts with an optimized composition demonstrate excellent reactivity in ethanol electrooxidation and capability in splitting C−C bonds and fully oxidizing ethanol to CO_2 (shown later). Therefore, it is of interest to explore the reactivity and selectivity of PtIrRh/SnO_2 and IrRh/SnO_2 catalysts in ethanol electrooxidation. Voltammetry scans of $PtRh_{1/3}$/SnO_2/C (with atomic ratio Pt/Rh/Sn of 1:$^1/_3$:1), PtIr/SnO_2/C (with atomic ratio Pt/Ir/Sn of 1:1:1), IrRh/SnO_2/C (with atomic ratio Ir/Rh/Sn of 1:1:1) and PtIrRh/SnO_2/C (with atomic ratio Pt/Ir/Rh/Sn of 1:1:1:1) catalysts are presented in Figure S3c. IrRh/SnO_2/C showed the highest oxide formation current and the most negative oxide reduction potential, due to the lower nobility of Ir and Rh with respect to Pt. As indicated in Figure 5c, the PtIr/SnO_2/C catalyst gave the lowest EOR onset potential among the four MM′/SnO_2/C catalysts, which is about 50 mV more negative compared to that of the $PtRh_{1/3}$/SnO_2/C catalyst, but the latter catalyst yields higher EOR current compared to that from PtIr/SnO_2/C when the applied potential is higher than ca. 0.42 V. We attribute the lower activity of PtIr/SnO_2/C in the high potential region to the fact that Ir tends to segregate on surfaces of PtIr nanoislands due to its greater oxophilicity with respect to Pt, resulting in a relatively higher Ir content at the surface than in the bulk composition and consequently a lower Pt content at the surface. Ir is easily oxidized at higher potentials, causing decreased ethanol adsorption and consequently reduced EOR activity. Surface science study of gas phase ethanol adsorption/decomposition on Ir(111) showed that ethanol adsorption is influenced by the presence of surface oxygen and the molecular ethanol desorption temperature was found to be ca. 20 K lower in the presence of adsorbed O (O_{ad}), indicating a weakened interaction between ethanol and Ir(111) in the presence of O_{ad}.[25] The PtIrRh/SnO_2 catalyst delivers lower current than both $PtRh_{1/3}$/SnO_2/C and PtIr/SnO_2/C, and the IrRh/SnO_2/C catalyst appears to be the poorest for EOR, as it is almost inactive.

To fully evaluate the activity and stability of PtIr/SnO_2/C and PtRh/SnO_2/C catalysts in ethanol electrooxidation, chronoamperometric (CA) measurements were carried out to examine the EOR activity of above two best ternary catalysts, PtIr/SnO_2/C (with atomic ratio Pt/Ir/Sn of 1:1:1) and $PtRh_{1/3}$/SnO_2/C (with atomic ratio Pt/Rh/Sn of 1:$^1/_3$:1). They were also compared with Pt/SnO_2/C, the best Pt-based binary electrocatalyst. As indicated in Figure 6, PtIr/SnO_2/C and $PtRh_{1/3}$/SnO_2/C demonstrate superior performance in ethanol electrooxidation, with greater reactivity and stability than that of Pt/SnO_2/C.

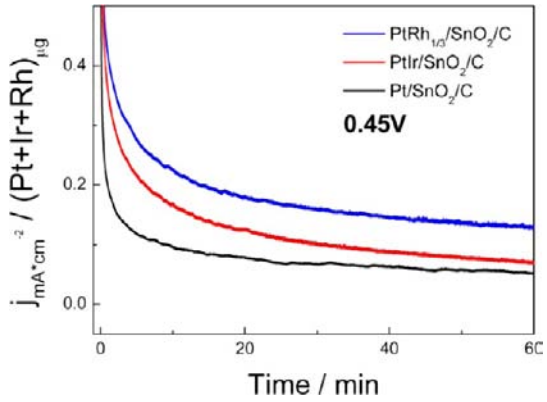

Figure 6. CA measurements at 0.45 V vs RHE of PtIr/SnO_2/C, $PtRh_{1/3}$/SnO_2/C and Pt/SnO_2/C electrocatalysts. Electrolyte: 0.5 M ethanol in 0.1 M $HClO_4$. All measurements were conducted at room temperature.

3.3. *In Situ* IRRAS Studies of MM′/SnO_2/C NP Electrocatalysts. *3.3.1. PtIr/SnO_2/C NP Electrocatalysts.* To gain insight on the reaction mechanisms of the ethanol electrooxidation reaction on the above catalysts, we carried out *in situ* IRRAS studies to reveal the reaction intermediates and product distribution information. The three PtIr/SnO_2/C electrocatalysts with different Pt/Ir/Sn ratios and four PtRh/SnO_2/C electrocatalysts with different Pt/Rh/Sn ratios were employed to establish the composition-selectivity correlation and to optimize catalyst composition. Figure 7 includes spectra recorded during EOR on PtIr/SnO_2/C, $PtRh_{1/3}$/SnO_2/C, and PtIrRh/SnO_2/C electrocatalysts, and additional spectra from the rest of the MM′/SnO_2/C electrocatalysts can be found in Figure S4. *In situ* IRRAS studies were also carried out with Pt/C and Pt/SnO_2/C catalysts for comparison (spectra not shown).

Figure 7a presents the recorded infrared spectra during ethanol electrooxidation on PtIr/SnO_2/C electrocatalyst with an atomic ratio Pt/Ir/Sn of 1:1:1, while the frequencies and detailed band assignments are listed in Table S2. Carbon dioxide (CO_2), acetic acid (CH_3COOH) and acetaldehyde (CH_3CHO) are the main products of ethanol oxidation in acidic solution. The positive-going peak near 2343 cm^{-1} is attributed to the asymmetric stretch vibration of CO_2, the product of ethanol total oxidation pathway. One can observe that the CO_2 band from the PtIr/SnO_2/C catalyst with an atomic ratio Pt/Ir/Sn of 1:1:1 shows a very high intensity, indicating the formation of large amounts of CO_2. The band located around 1705 cm^{-1} can be assigned to the stretch vibration of the C═O bond, found in both acetaldehyde and acetic acid. The band at 1598 cm^{-1} represents the H−O−H deformation of adsorbed water molecules. The C═O stretching mode of adsorbed acetaldehyde and acetyl around 1620−1635 cm^{-1} cannot be resolved because of the presence of the strong water band. The bands at 1350 cm^{-1} and around 1396−1410 cm^{-1} are assigned to CH_3 in-plane bending mode and O−C−O stretching of adsorbed acetate, respectively. These two bands are close and difficult to distinguish. A well-defined band at 1280 cm^{-1} is the characteristic absorption of C−O stretching in acetic acid, which is usually employed for quantitative analysis of acetic acid. The C−H wagging vibration

dx.doi.org/10.1021/ja306384x | J. Am. Chem. Soc. 2013, 135, 132−141

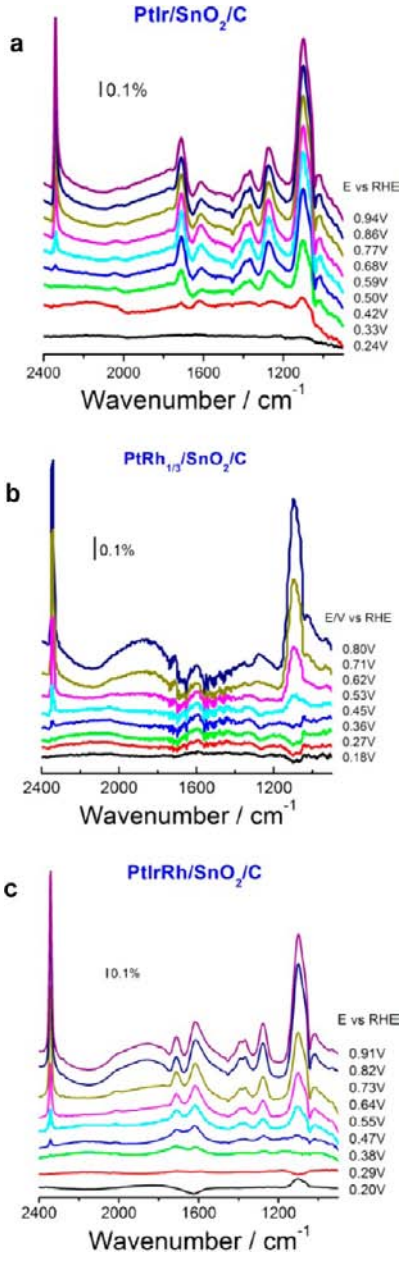

Figure 7. *In situ* IRRAS spectra recorded during EOR on three MM′/SnO_2/C NP electrocatalysts: (a) PtIr/SnO_2/C, (b) $PtRh_{1/3}$/SnO_2/C, and (c) PtIrRh/SnO_2/C.

in CH_3CHO, at 1108 cm^{-1}, overlaps with the strong band at 1110 cm^{-1} of Cl−O stretching in ClO_4^-. The strong band for ClO_4^- ions is the consequence of its accumulation in the thin layer cell to compensate the charge at the electrode surface under increasingly positive electrode potential. The downward band at 1044 cm^{-1} is the signature peak for the C−O stretching vibration of CH_3CH_2OH, representing the consumption of ethanol by oxidation. The band observed at 933 cm^{-1} is assigned to C−C−O asymmetric stretching of acetaldehyde, which is used for quantification of acetaldehyde in this study.

To better compare the selectivity of the three PtIr/SnO_2/C electrocatalysts and to understand the effect of Ir content on the catalysts' capability in C−C bond cleavage, the variation of integrated band intensities of CO_2 (2343 cm^{-1}), CH_3CHO (933 cm^{-1}) and CH_3COOH (1280 cm^{-1}) with applied potential were obtained from all the spectra (Figure 7a, Figure S4a,b). CO_2 produces the strongest band in the spectra of PtIr/SnO_2/C with atomic ratio Pt/Ir/Sn of 1:1:1, while CH_3COOH bands show higher intensity on the other two PtIr/SnO_2 catalysts (with atomic ratio Pt/Ir/Sn of $1:^1/_2:1$ and $1:^1/_4:1$). CH_3CHO is only produced in small amounts at all three PtIr/SnO_2/C catalysts. The EOR total oxidation current efficiency, defined as the ratio between charge contribution from total oxidation pathway (C_{CO_2}) and charge contribution from both total oxidation and partial oxidation pathways ($C_{CO_2+CH_3COOH+CH_3CHO}$), could directly represent the capability of the catalysts to split the C−C bond. Its variation versus applied potential is plotted in Figure 8a.

The quantity of different oxidation products is determined using a published method.[40−42] In short, the yield of oxidation products are calculated using respective integrated band intensities, and the amount of a given species Q (mol/cm^2) inside the thin layer cavity follows the relationship[37]

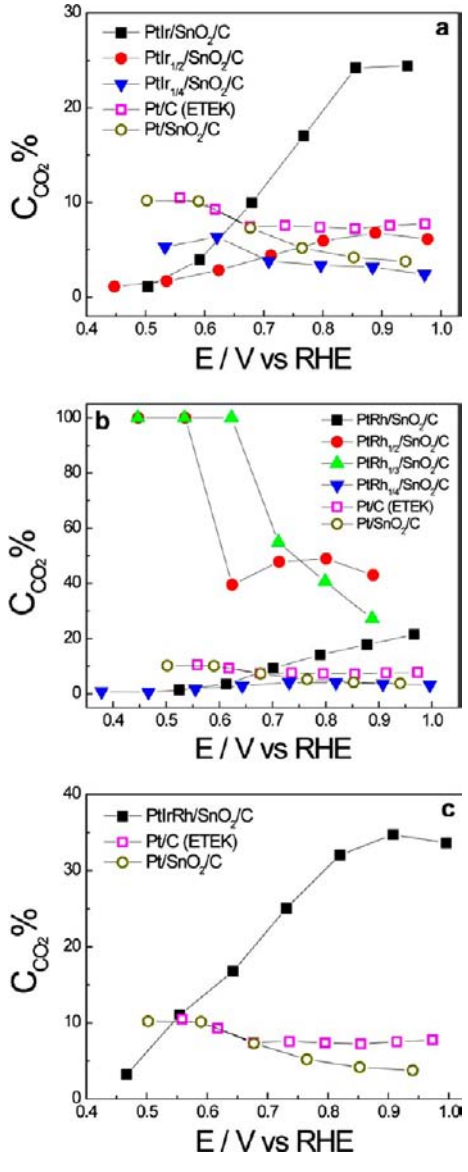

Figure 8. The variation of different MM′/SnO_2/C catalysts' EOR total oxidation current efficiency, i.e., $C_{CO_2}/C_{CO_2+CH_3COOH+CH_3CHO}$, versus applied potential.

dx.doi.org/10.1021/ja306384x | J. Am. Chem. Soc. 2013, 135, 132−141

$$Q = \frac{A_i}{\varepsilon_{eff}} \quad (1)$$

where A_i is the respective integrated band intensity and ε_{eff} is the value of the effective absorption coefficient. Values of ε_{eff} are taken from the work of Weaver et al.,[41,42] and these are 3.5×10^4, 5.8×10^3, and 2.2×10^3 M^{-1} cm^{-2} for CO_2, CH_3COOH, and CH_3CHO, respectively. The production of one CO_2, CH_3COOH, and CH_3CHO molecule released 6, 4, and 2 electrons, respectively. Therefore, $C_{CO_2}/C_{CO_2+CH_3COOH+CH_3CHO}$ are calculated using the following equation:

$$\frac{C_{CO_2}}{C_{CO_2} + C_{CH_3COOH} + C_{CH_3CHO}} = \frac{6 \cdot Q_{CO_2}}{6 \cdot Q_{CO_2} + 4 \cdot Q_{CH_3COOH} + 2 \cdot Q_{CH_3CHO}} \quad (2)$$

Figure 8a shows the ethanol total oxidation current efficiency change versus applied potential during ethanol electro-oxidation on three $PtIr/SnO_2$ catalysts. The catalyst with highest Ir content, $PtIr/SnO_2/C$ catalyst with atomic ratio Pt/Ir/Sn of 1:1:1, gives reasonably enhanced selectivity toward CO_2 formation compared to pure Pt/C and binary $Pt/SnO_2/C$, while the other two $PtIr/SnO_2/C$ NP catalysts show a lowered capability in C−C bond splitting compared to pure Pt.

It is interesting to observe that the $PtIr/SnO_2$ catalysts' selectivity to CO_2 is very sensitive to the Ir concentration. At this moment, we can only speculate that it is caused by necessity for optimal ensemble of Ir atoms that can accomplish a sufficiently strong adsorption of ethanol and the C−C bond splitting.

3.3.2. PtRh/SnO$_2$/C NP Electrocatalysts. Our combined theoretical and experimental studies have demonstrated ternary Pt−Rh−SnO_2 system could break C−C bond and fully oxidize ethanol to CO_2. The four $PtRh/SnO_2/C$ electrocatalysts with different Pt/Rh ratios were employed to establish composition-selectivity correlation and to optimize the catalysts' composition, which is of great importance because: (i) high EOR activity and high selectivity toward CO_2 formation are both essential goals in ethanol electrocatalysis; (ii) Rh is a very rare and expensive material and Rh alone is not active for ethanol electro-oxidation.

Figure 7b displays infrared spectra collected from the $PtRh_{1/3}/SnO_2/C$ electrocatalyst during EOR and the spectra from the other three $PtRh/SnO_2/C$ electrocatalysts can be found in Figure S4c−e. Similar to the ones from $PtIr/SnO_2/C$ catalysts, CO_2, CH_3COOH and CH_3CHO are clearly identified from all spectra, suggesting the parallel reaction pathways take place on all of the above $PtRh/SnO_2$ catalysts. To better understand the effect of the Rh component on the catalysts' selectivity toward C−C bond cleavage and CO_2 production, the variation of integrated band intensities of CO_2 (2343 cm^{-1}), CH_3CHO (933 cm^{-1}), and CH_3COOH (1280 cm^{-1}) with applied potential for all $PtRh/SnO_2/C$ catalysts was determined. Figure 8b shows ethanol total oxidation current efficiency change versus applied potential during ethanol electro-oxidation on four $PtRh/SnO_2$ catalysts. One can find the $PtRh/SnO_2$ catalyst with a moderate Rh content (with atomic ratio Pt/Rh/Sn of 1:$^1/_2$:1 and 1:$^1/_3$:1) gives the best selectivity for C−C bond splitting and CO_2 formation, while the other two $PtRh/SnO_2/C$ NP catalysts (with atomic ratio Pt/Rh/Sn of 1:1:1 and 1:$^1/_4$:1) show lowered capability for C−C bond splitting compared to pure Pt.

One can find, in the potential region of practical interest (i.e., lower than 0.7 V), the total oxidation current efficiency for the two best $PtRh/SnO_2/C$ catalysts ($PtRh_{1/3}/SnO_2/C$ and $PtRh_{1/2}/SnO_2/C$) is above 40%. To the best of our knowledge, these catalysts have achieved the highest ethanol conversion efficiency of all known ethanol oxidation catalysts. Therefore, the catalysts' selectivity is highly dependent on their composition, that is, Pt/Rh ratio, and a moderate Rh content yields the highest selectivity to CO_2. We attribute this phenomenon to both the geometric "ensemble effect" and the electronic "ligand effect". DFT calculations propose an optimum pathway for C−C bond breaking at the Rh,Pt/SnO_2 interface: $*CH_3CH_2OH \rightarrow *CH_3CHO + H^* \rightarrow *CH_2CH_2O + 2H^* \rightarrow *CH_2 + *CH_2O + 2H^*$.[18] The dehydrogenation process is favored on Pt sites, while C−C bond cleavage prefers Rh sites. One can find that multiple adjacent Pt sites are required for abstracting atomic hydrogen in ethanol molecules; therefore, a higher Pt content than Rh content is desired in this system. When the Rh content is too low, like in the $PtRh_{1/4}/SnO_2/C$ catalyst, there are not enough Rh sites for the C−C bond splitting reaction. Moreover, the metal-CH_2CH_2O reaction leading to C−C bond breaking is facilitated by back-donation from the π orbitals of $*CH_2CH_2O$ to the d orbital of the metal atoms, and Rh is a better candidate than Pt because of its electronic structure. In a mixture of Pt and Rh, the strong interaction between the two elements is accompanied by an electron transfer from Rh to Pt and more d-states of Rh become available above the Fermi level. This suggests that in the PtRh system, Rh can be more active while Pt becomes more inert, which promotes bond cleavage on Rh sites and simultaneously prevents ethanol partial oxidation on Pt sites. Thus, these results imply that a suitably higher amount of Pt could empty more d-states of Rh, thereby improving the selectivity to total oxidation.

3.3.3. PtIrRh/SnO$_2$/C NP Electrocatalyst. Figure 7c shows infrared spectra generated on the $PtIrRh/SnO_2/C$ catalyst and Figure 8c presents its ethanol total oxidation current efficiency determined from the infrared study. At high overpotential, this catalyst gives a considerably higher CO_2 production rate; however, it is still lower than the best $PtRh/SnO_2/C$ catalysts. In summary, the CO_2 production efficiency of the catalysts decreases in the order: $PtRh/SnO_2/C$ (with atomic ratio Pt/Rh/Sn of 1:$^1/_3$:1 and 1:$^1/_2$:1) > $PtIrRh/SnO_2/C$ (with atomic ratio Pt/Ir/Rh:Sn of 1:1:1:1) > $PtIr/SnO_2/C$ (with atomic ratio Pt/Ir/Sn of 1:1:1).

It must be noted that the employment of the IRRAS technique in quantitative studies has several limitations: (i) The accumulation and diffusion of EOR products occur at the same time, and the detected signal must be treated as the total amount of product minus the amount that diffuses away from the thin-layer. Different products, such as CO_2, CH_3COOH and CH_3CHO, are expected to have different diffusion rates when leaving the thin-layer. CO_2 is the most volatile among the three major products, so one would expect that CO_2 diffuses faster than CH_3COOH and CH_3CHO. (ii) In the thin-layer, reaction products are likely to be readsorbed and further oxidized, which could be different from the case in a real fuel cell environment. (iii) It has been claimed that CH_4 could also be an EOR product because part of $-CH_3$ fragments in CH_3CH_2OH molecules are not oxidized to CO_2, but instead are reduced to CH_4 in hydrogen underpotential deposition

dx.doi.org/10.1021/ja306384x | J. Am. Chem. Soc. 2013, 135, 132−141

region and then desorbed from the catalyst surface. The IRRAS study here appears to be not very useful in detecting CH_4, which could cause an imprecise determination of current efficiency. (iv) The measurements reproducibility may be affected by an uneven electrode surface (prepared by casting NP catalysts ink on an Au disk). The resulting electrolyte layer of nonuniform thickness and the strong IR absorption by the amorphous carbon support.

On-line differential electrochemical mass spectroscopy (DEMS) has been accepted as a quantitative tool to determine ethanol electro-oxidation products.[15−17] The Pt/SnO_2 catalyst shows lower CO_2 production than that on pure Pt catalyst, which is consistent with literature reports from both on-line DEMS and *in situ* FTIR studies.[15−17] However, the CO_2 production current efficiency on pure Pt, 5−10% as indicated in our IRRAS studies, is considerably higher than the values determined from DEMS measurements, which are mostly in the range of 2−3%. Moreover, our IRRAS studies observe a very low production of CH_3CHO, while DEMS determines a considerable higher CH_3CHO generation (average current efficiency around 37% for CH_3CHO) in a similar electrolyte.[15,17] We attribute the different results from the two techniques, IRRAS and DEMS, to their different reaction environments: thin-layer cell versus flow cell. In the thin-layer configuration, CH_3CHO is more likely to be readsorbed on catalyst surface and be further oxidized to CO_2 or CH_3COOH, while in the flow-cell setup in DEMS studies, CH_3CHO could easily desorb from catalyst surface once it formed. Nevertheless, on-line DEMS could be a very important complement to the *in situ* IRRAS study, and currently the DEMS studies are underway in our lab to gain more information in catalysts' selectivity.

On the basis of the behavior of two types of ternary electrocatalysts for the EOR, some features and commonalities appear to provide guidelines for their effective design. First, such a multicomponent catalyst has to provide a facile adsorption of ethanol, that is, it has to have a metallic surface with sizable ensembles of atoms. The second constituent may be more oxophilic than the first, but its OH adsorption has to be weak enough to permit suppression by lateral repulsion from OH or O from the oxide component, such as SnO_2.

3.4. *In Situ* XAS Study of the $PtIr/SnO_2/C$ Electrocatalyst. *In situ* XAS studies of ternary $Pt-Rh-SnO_2$ electrocatalysts have been discussed elsewhere;[18,19] therefore, only the results from *in situ* XAS study of the $PtIr/SnO_2/C$ electrocatalyst are discussed in this study. *In situ* XANES spectra obtained from the $PtIr/SnO_2/C$ electrocatalyst (with atomic ratio Pt/Ir/Sn of 1:1:1) are presented in Figure 9. The L3 absorption edges of Pt and Ir are very close; hence, the XANES feature of Pt L3 edge has a mixed impact from Ir L3 edge absorption. The much higher white line observed from Ir L3 edge compared to Ir black reference (not shown) at all applied potentials indicates an oxidized state of Ir. Both Ir and Pt spectra show a potential dependence; they start to be more oxidized when the potential increases. The ratio between the absorption intensities of Pt and Ir is ca. 0.95, measured from the XAS spectra. The difference between the absorption intensities approximates the composition of the Pt/Ir electrocatalyst because of the proximity of Pt and Ir absorption coefficients, so we determined the Pt/Ir ratio is close to 1, which is consistent with the nominal value.[43,44]

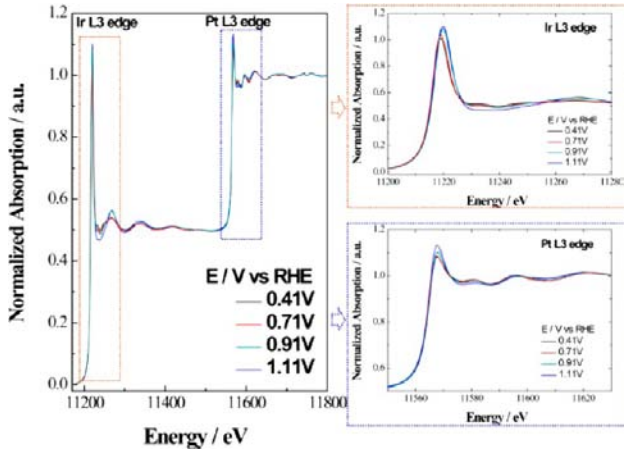

Figure 9. *In situ* XANES spectra of Pt L3 and Ir L3 edges of $PtIr/SnO_2/C$ electrocatalyst under different applied potentials.

4. CONCLUSIONS

Carbon-supported ternary MM'/SnO_2 NP electrocatalysts comprising SnO_2 NP cores decorated with multimetallic nanoislands (MM′ = PtIr, PtRh, IrRh, PtIrRh) were prepared using a seeded growth approach as synthetic analogues to the $PtRh/SnO_2(110)$ model catalyst in our DFT study. An array of characterization techniques, XRD, Z-contrast AC-STEM, EDS and *in situ* XAS, were employed to establish the composition and architecture of the synthesized NPs.

A combination of electrochemical measurements and *in situ* IRRAS was used to investigate the catalytic properties of the MM'/SnO_2 NP electrocatalysts for ethanol electro-oxidation. Both EOR reactivity and selectivity toward CO_2 formation of several of these $MM'SnO_2/C$ NP catalysts are significantly higher than those of Pt/C and $Pt/SnO_2/C$. Among the systems studied, $PtIr/SnO_2/C$ catalyst with highest Ir content, that is, the catalyst with atomic ratio Pt/Ir/Sn = 1:1:1, showed the most negative EOR onset potential and considerably improved capability for C−C bond splitting. $PtRh/SnO_2/C$ electrocatalysts with a suitable Rh content, that is, catalysts with atomic ratio Pt/Rh/Sn = $1:^1/_2:1$ and $1:^1/_3:1$, exhibit the highest selectivity toward ethanol total oxidation. We attribute this effect to both ensemble effect and ligand effect. The $PtIrRh/SnO_2/C$ electrocatalyst (with atomic ratio Pt/Ir/Rh/Sn of 1:1:1:1) displays lower activity compared to $PtRh/SnO_2/C$ and $PtIr/SnO_2/C$ electrocatalysts, and the $IrRh/SnO_2/C$ electrocatalyst (with atomic ratio Ir/Rh/Sn of 1:1:1) is the poorest of all. The CO_2 production efficiency of the above catalysts decreases in the following order: $PtRh/SnO_2$ (with atomic ratio Pt/Rh/Sn of $1:^1/_2:1$ and $1:^1/_3:1$) > $PtIrRh/SnO_2$ (with atomic ratio Pt/Ir/Rh/Sn of 1:1:1:1) > $PtIr/SnO_2$ (with atomic ratio Pt/Ir/Sn of 1:1:1).

The findings presented in this paper can improve our understanding of the EOR electrocatalysis and help in designing novel nanostructured materials with enhanced activity and selectivity in ethanol electrooxidation.

■ ASSOCIATED CONTENT

Supporting Information

AC-STEM images (Figure S1) and EDS mapping (Figure S2) of $PtRh_{1/2}/SnO_2/C$ and $PtRh_{1/3}/SnO_2/C$ catalysts; CV curves of all nanocatalysts in 0.1 M $HClO_4$ (Figure S3); *in situ* IRRAS spectra collected from several $PtIr/SnO_2/C$ and $PtRh/SnO_2/C$

dx.doi.org/10.1021/ja306384x | *J. Am. Chem. Soc.* 2013, 135, 132−141

catalysts during EOR (Figure S4); ICP-OES results (Table S1); IR band assignments (Table S2). This material is available free of charge via the Internet at http://pubs.acs.org.

AUTHOR INFORMATION

Corresponding Author

adzic@bnl.gov

Notes

The authors declare no competing financial interest.

ACKNOWLEDGMENTS

This research was performed at Brookhaven National laboratory under contract DE-AC02-98CH10886 with the US Department of Energy, Division of Chemical Sciences, Geosciences and Biosciences Division. This work was supported by the Fuel Cell Technologies Program, Office of Energy Efficiency and Renewable Energy, U.S. Department of Energy under Award Number DE-EE0000456 and ORNL's ShaRE User Facility, Office of Basic Energy Sciences, U.S. Department of Energy.

REFERENCES

(1) Edwards, J. K.; Thomas, A.; Solsona, B. E.; Landon, P.; Carley, A. F.; Hutching, G. J. *Catal. Today* **2007**, *122*, 297.

(2) Wasmus, S.; Kuver, A. *J. Electroanal. Chem.* **1999**, *461*, 14.

(3) Kordesch, K.; Simader, G. *Fuel Cells and Their Applications*; VCH Verlag GmbH: Weinheim, 1996.

(4) Lamy, C.; Coutanceau, C.; Leger, J.-M. The Direct Ethanol Fuel Cell: A Challenge To Convert Bioethanol Cleanly into Electric Energy. In *Catalysis for Sustainable Energy Production*; Barbaro, P., Bianchini, C., Eds.; WILEY-VCH Verlag GmbH & Co. kGaA: Weinheim, 2009; pp 1−42.

(5) Lamy, C.; Belgsir, E. M.; Leger, J.-M. *J. Appl. Electrochem.* **2001**, *31*, 799.

(6) Antolini, E. *J. Power Sources* **2007**, *170*, 1.

(7) Song, S.; Tsiakaras, P. *Appl. Catal., B* **2006**, *63*, 187.

(8) Lamy, C.; Rousseau, S.; Belgsir, E. M.; Coutanceau, C.; Leger, J.-M. *Electrochim. Acta* **2004**, *49*, 3901.

(9) Du, W.; Wang, Q.; LaScala, C. A.; Zhang, L.; Su, D.; Frenkel, A. I.; Mathura, V. K.; Teng, X. *J. Mater. Chem.* **2011**, *21*, 8887.

(10) Du, W.; Wang, Q.; Saxner, D.; Aaron Deskins, N.; Su, D.; Krzanowski, J. E.; Frenkel, A. I.; Teng, X. *J. Am. Chem. Soc.* **2011**, *133* (38), 15172−15183.

(11) Zhou, W.-P.; Axnanda, S.; White, M. G.; Adzic, R. R.; Hrbek, J. *J. Phys. Chem. C* **2011**, *115*, 16467−16473.

(12) Kowal, A.; Gojkovic, S. Lj.; Lee, K.-S.; Olszewski, P.; Sung, Y.-E. *Electrochem. Commun.* **2009**, *11*, 724−727.

(13) Weickowski, A.; Sobrowski, J.; Zelenay, P.; Franaszczuk, K. *Electrochim. Acta* **1981**, *26*, 1622.

(14) De Souza, J. P. I.; QueirOZ, S. L.; Bergamaski, K.; Gonzalez, E. R.; Nart, F. C. *J. Phys. Chem. B* **2002**, *106*, 9825.

(15) Wang, Q.; Sun, G. Q.; Jiang, L. H.; Xin, Q.; Sun, S. G.; Jiang, Y. X.; Shen, S. P.; Jusys, Z.; Behm, R. J. *Phys. Chem. Chem. Phys.* **2007**, *9*, 2686.

(16) Iwasita, T.; Pastor, E. *Electrochim. Acta* **1994**, *39*, 531.

(17) Wang, H.; Jusys, Z.; Behm, R. J. *J. Power Sources* **2006**, *154*, 351.

(18) Kowal, A.; Li, M.; Shao, M.; Sasaki, K.; Vukmirovic, M. B.; Zhang, J.; Marinkovic, N. S.; Liu, P.; Frenkel, A. I.; Adzic, R. R. *Nat. Mater.* **2009**, *8*, 325.

(19) Li, M.; Kowal, A.; Sasaki, K.; Marinkovic, N.; Su, D.; Korach, E.; Liu, P.; Adzic, R. R. *Electrochim. Acta* **2010**, *55* (14), 4331−4338.

(20) Resta, A.; Blomquist, J.; Gustafson, J.; Karhu, H.; Mikkelsen, A.; Lundgren, E.; Uvdal, P.; Andersen, J. N. *Surf. Sci.* **2006**, *600*, 5136−5141.

(21) Resta, A.; Gustafson, J.; Westerstr, R.; Mikkelsen, A.; Lundgren, E.; Andersen, J. N.; Yang, M.-M.; Ma, X.-F.; Bao, X.-H.; Li, W.-X. *Surf. Sci.* **2008**, *602*, 3057−3063.

(22) Idriss, H. *Platinum Met. Rev.* **2004**, *48*, 105−115.

(23) Choi, Y.; Liu, P. *Catal. Today* **2011**, *165* (1), 64−70.

(24) de Tacconi, N. R.; Lezna, R. O.; Beden, B.; Hahn, F.; Lamy, C. *J. Electroanal. Chem.* **1994**, *379*, 329−337.

(25) Weststrate, C. J.; Ludwig, W.; Bakker, J. W.; Gluhoi, A. C.; Nieuwenhuys, B. E. *ChemPhysChem* **2007**, *8*, 932−937.

(26) Cao, L.; Sun, G.; Li, H.; Xin, Q. *Electrochem. Commun.* **2007**, *9*, 2541−2546.

(27) Sasaki, K.; Wang, J. X.; Naohara, H.; Marinkovic, N.; More, K.; Adzic, R. R. *Electrochim. Acta* **2010**, *55* (8), 2645−2652.

(28) Ravel, B.; Newville, M. *J. Sychrotron Radia.* **2005**, *12*, 537.

(29) Jiang, L.; Sun, G.; Zhou, Z.; Sun, S.; Wang, Q.; Yan, S.; Li, H.; Tian, J.; Guo, J.; Zhou, B.; Xin, Q. *J. Phys Chem. B* **2005**, *109*, 8774−8778.

(30) Zhang, H.; Du, N.; Chen, B.; Cui, T.; Yang, D. *Mater. Res. Bull.* **2008**, *43*, 3164−3170.

(31) Alayoglu, S.; Nilekar, A. U.; Mavrikakis, M.; Elchhorn, B. *Nat. Mater.* **2008**, *7*, 333−338.

(32) Nilekar, A. U.; Alayoglu, S.; Eichhorn, B.; Mavrikakis, M. *J. Am. Chem. Soc.* **2010**, *132*, 7418−7428.

(33) Peng, Z.; Yang, H. *Nano Today* **2009**, *4*, 143−164.

(34) Peng, Z.; Yang, H. *Nano Res.* **2009**, *2*, 406−415.

(35) Wang, C.; Vliet, D. V. D.; More, K. L.; Zaluzec, N. J.; Peng, S.; Sun, S.; Daimon, H.; Wang, G.; Greeley, J.; Pearson, J.; Paulikas, A. P.; Karapetrov, G.; Strmcnik, D.; Markovic, N. M.; Stamenkovic, V. R. *Nano Lett.* **2011**, *11*, 919−926.

(36) Wang, C.; Xu, C.; Zeng, H.; Sun, S. *Adv. Mater.* **2009**, *21*, 3045−3052.

(37) Hansen, M.; Anderko, K., *Constitution of Binary Alloys*, 2nd ed.; McGraw-Hill Book Company: New York, 1958.

(38) Selbach, E.; Jacques, H.; Eiermann, K.; Lengeler, B.; Schilling, W. *Thin Solid Films* **1987**, *149* (1), 17−28.

(39) Zhou, W.-P.; Li, M.; Koenigsmann, C.; Ma, C.; Wong, S. S.; Adzic, R. R. *Electrochim. Acta* **2011**, *56* (27), 9824−9830.

(40) Camara, G. A.; Iwasita, T. *J. Electroanal. Chem.* **2005**, *578*, 315−321.

(41) Leung, L.-W. H.; Chang, S.-C.; Weaver, M. J. *J. Electroanal. Chem.* **1989**, *266*, 317.

(42) Gao, P.; Chang, S.-C.; Zhou, Z.; Weaver, M. J. *J. Electroanal. Chem.* **1989**, *272*, 161.

(43) Zhang, J.; Sasaki, K.; Sutter, E.; Adzic, R. R. *Science* **2007**, *315*, 220−222.

(44) Karan, H. I.; Sasaki, K.; Kuttiyiel, K. A.; Farberow, C. A.; Mavrikakis, M.; Adzic, R. R. *ACS Catal.* **2012**, *2* (5), 817−824.